Measurement of the ^{80}Se(γ, n) reaction with linearly polarized γ rays

S. A. Yates,[*] B. Fallin,[†] C. R. Howell,[‡] Krishichayan,[§] and W. Tornow[‖]

Department of Physics and Triangle Universities Nuclear Laboratory, Duke University, Durham, North Carolina 27708, USA

S. M. Grimes[¶]

Department of Physics, Ohio University, Athens, Ohio 45701, USA

This paper reports the results of the first measurements of the differential cross section of the ^{80}Se(γ, n)^{79}Se reaction with a linearly polarized gamma-ray (γ-ray) beam. The cross section was measured at three incident γ-ray beam energies: 15.6, 15.8, and 16.0 MeV, with a beam energy spread of 3.0% full width at half-maximum (FWHM). The differential cross section for the excitation spectrum in ^{79}Se was measured at two scattering angles in the plane of the beam polarization: $\theta = 90°$ and $135°$, and at one angle in the plane perpendicular to the plane of polarization: $\theta = 90°$. The total photoneutron cross sections determined from these data are between 0.8 and 1.3 standard deviations smaller than previously published results. The excitation spectra measured in this work were fit with a Hauser-Feshbach model. Better fits to the data were obtained with a constant-temperature formulation of the nuclear level density (NLD) than with a Fermi-gas NLD model. The parameters for the constant-temperature NLD model obtained in this work are consistent with those obtained for medium-mass nuclei in previous studies.

I. INTRODUCTION

More than half of the heavy nuclei ($A > 60$) are produced in stars by s-process nucleosynthesis—nuclear reactions driven by slow neutron capture [1]. In some mass regions, the relative abundances of stable nuclei produced in stellar nucleosynthesis are highly sensitive to the rates of β decay and neutron capture on branch-point isotopes [2,3]. For example, ^{79}Se is a branch-point isotope in the synthesis of stable krypton isotopes (e.g., ^{80}Kr, ^{82}Kr, and ^{83}Kr [4,5]). Neutron capture on ^{79}Se is part of a reaction path that produces ^{82}Kr without formation of ^{80}Kr [5]. The relative rates of β decay of ^{79}Se and neutron capture on ^{79}Se determine the ratio of the abundances of ^{80}Kr and ^{82}Kr. In the stellar environment, a bath of photons with energies corresponding to the temperature of the star produces a distribution of initial states, upon which nuclear reactions are then induced. For this reason, the effective reaction rate of ^{79}Se(n, γ) in stellar nucleosynthesis depends, among other factors [6–8], on the nuclear level density (NLD) of ^{79}Se [9]. The (γ, n) time-reversed photodisintegration reaction offers a mechanism for determining the neutron capture cross section and level density of radioactive nuclei, in this case ^{79}Se.

The cross section for neutron capture on ^{79}Se also has applications in transmutation of nuclear waste [5,10]. With a

radioactive half-life of $T_{1/2} = 326$ ky by β decay [11], ^{79}Se is among the longest-lived isotopes produced in nuclear fission. In nuclear waste transmutation methods based on irradiation of materials with a high flux of neutrons, ^{79}Se nuclei are transformed to stable ^{80}Se via a single neutron capture reaction. The development of accurate computer simulations of nuclear waste transmutation systems requires accurate cross-section data for neutron-induced reactions (e.g., neutron capture).

In this paper, we report the first measurements of angle-correlated and energy-dependent differential cross sections for the ^{80}Se(γ, n)^{79}Se reaction. The measurements were performed using a linearly polarized gamma-ray (γ-ray) beam from the High Intensity Gamma-ray Source (HIGS) at the Triangle Universities Nuclear Laboratory (TUNL). Measurements were made at three incident γ-ray beam energies: 15.6, 15.8, and 16.0 MeV. The data were analyzed using the angular correlation reaction formalism described by Weller *et al.* [12,13] to determine the γ-ray transition reduced matrix elements. The orbital angular momentum transfer was constrained to be $\ell = 0$ or 1 in the analysis (see Fig. 1). The matrix elements were then used to compute the angle-integrated differential cross section as a function of the excitation energy in the residual ^{79}Se nucleus. The total (γ, n) reaction cross sections determined from the excitation data measured in this work are compared to previously published cross sections [14,15]. The excitation data were fitted with a Hauser-Feshbach statistical nuclear model [16,17] to determine the nuclear level density (NLD) model that best represents the data (see general discussions of NLD models in Refs. [9,18,19]).

Section II describes the experimental technique used to perform the measurements. Section III presents the data

[*]stephen.yates@duke.edu
[†]fallin@tunl.duke.edu
[‡]howell@tunl.duke.edu
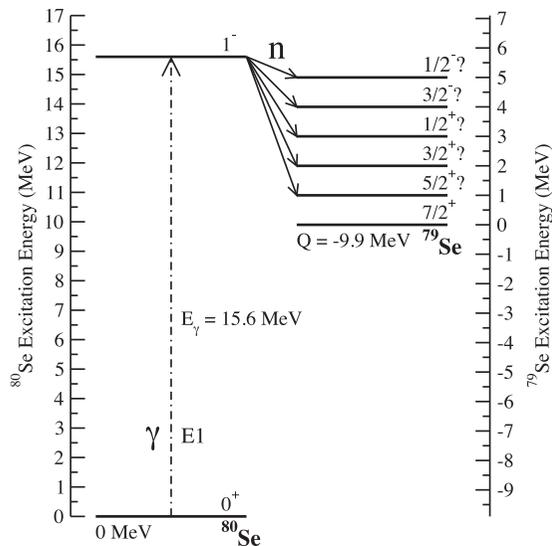[§]krishi@tunl.duke.edu
[‖]tornow@tunl.duke.edu
[¶]grimes@ohio.edu

FIG. 1. Energy level diagram of the $^{80}\text{Se}(\gamma, n)^{79}\text{Se}$ reaction. A $J^\pi = 1^-$ state in ^{80}Se is excited by an $E1$ γ-ray transition from the 0^+ ground state. The Q value of the reaction is -9.9 MeV. For the incident γ-ray beam energies used in this experiment, the emitted neutron leaves the residual ^{79}Se nucleus in states with excitation energies from just above 0 (the ground state) up to about 6 MeV. The J^π states shown for ^{79}Se are for the emission of $\ell = 0$ or 1 neutrons. The energy levels depicted for these states are hypothetical examples of possible excitations, as indicated by the "?" marks next to the J^π labels.

analysis, including the determination of the γ-ray transition reduced matrix elements from the measured angle-correlated differential cross sections and the determination of the angle-integrated differential cross section using these reduced matrix elements. Section IV compares our data to statistical model calculations, including the estimation of the total (γ, n) reaction cross section from the differential data and the fit of the excitation spectrum to a Hauser-Feschbach model for the level density of ^{79}Se. Section V summarizes the results and findings.

II. EXPERIMENTAL TECHNIQUE

The γ-ray beam at HIGS is produced by Compton backscattering of photons inside the optical cavity of a free-electron laser (FEL) off relativistic electron bunches circulating in a storage ring. Descriptions of the facility and the research program are given in a paper by Weller *et al.* [20]. The diameter of the collimator selects the cross-sectional intensity profile of the γ-ray beam and determines the energy spread of the beam. The distance from the electron-photon collision point to the collimator is approximately 53 m. This arrangement of the electron beam and collimator produces a γ-ray beam with an energy profile that has a Gaussian shape with a slight low-energy tail. In this work, the collimator was made of aluminum, had a circular opening of 1.25 cm diameter, and was 44.45 cm long. With this collimator, the energy spread of the γ-ray beam incident on the target was 3.0% full width at half-maximum (FWHM). A plot of
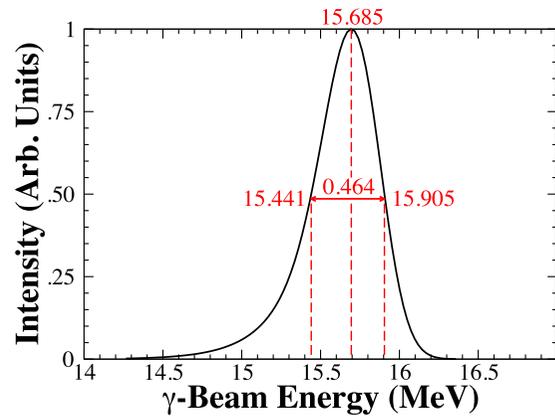

FIG. 2. Simulated flux profile for the 15.6-MeV γ-ray beam used in this experiment. The energy spread is 3.0% FWHM. The y axis is normalized to the peak energy flux and denoted in arbitrary units. These data were obtained using the simulation developed by Sun and Wu [21].

the simulated γ-ray beam energy profile for this collimator is shown in Fig. 2. The simulations were performed using software developed by Sun and Wu [21]. The 15.6-MeV γ-ray beam was produced by Compton backscattering of FEL photons with wavelength 454.7 nm off 624-MeV electrons. The relative rms energy spread in the electron beam was 4.5×10^{-3}. The average γ-ray beam flux on target for these measurements was 3×10^7 γ/s. The γ-ray beam at the HIGS is pulsed with a bunch width of 300 ps FWHM and a period of 180 ns between pulses. This time structure enables neutron energy determinations by time-of-flight (TOF) methods.

Cross-section measurements of the $^{80}\text{Se}(\gamma, n)$ reaction were performed at three incident γ-ray beam energies, with centroids of 15.6, 15.8, and 16.0 MeV. Schematic diagrams of the top and front views of the experimental setup are shown in Figs. 3 and 4, respectively. An isotopic-enriched ^{80}Se target
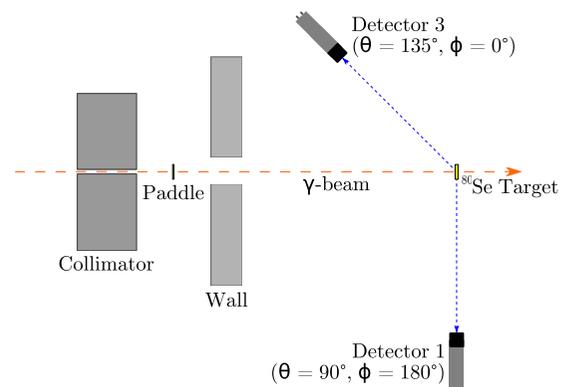

FIG. 3. Experimental setup as seen by an overhead observer. Only the detectors located in the plane of the beam polarization axis are shown. Detector 2 (not shown) is directly below the target. The scattering angle (θ) and azimuthal angle (ϕ) of the detectors are labeled in the drawing. The distances from the detectors to the target and the relative dimensions of the detectors and sample are to scale. The remainder of the drawing is not to scale.
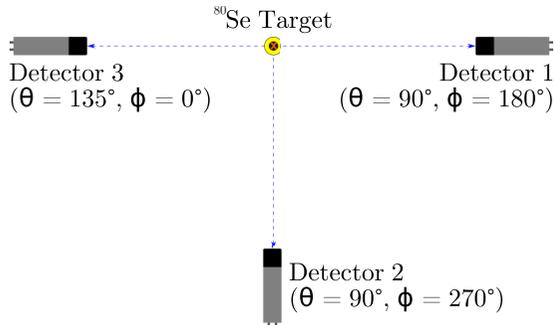
FIG. 4. Experimental setup as seen by an observer located upstream of the target and looking along the γ-ray beam path toward the target. The scattering (θ) and azimuthal (ϕ) angles of the detectors are labeled in the diagram. Detector 3 is out of the plane containing the target and Detectors 1 and 2. The distances from the detectors to the target and the relative dimensions of the detectors and sample are to scale.

was bombarded with a pulsed, collimated, linearly polarized beam. The polarization of the beam was in the horizontal plane. Three liquid-scintillation detectors filled with BC501-A fluid were placed around the target, as shown in Figs. 3 and 4. This scintillator fluid was used because of its excellent neutron-γ pulse shape discrimination (PSD) properties. The energies of the detected neutrons were determined using the TOF technique, with the peak in the TOF spectrum due to the prompt γ rays as the fixed time reference.

A thin plastic scintillator paddle just after the exit of the collimator was used to monitor the beam flux incident on the target. The absolute detection efficiency of the paddle was calibrated relative to the efficiency of an HPGe detector (110% efficiency relative to a 3-in. diameter $\times$ 3-in. thick NaI detector). This detector could be moved in and out of the γ-ray beam path. The absolute efficiency of the HPGe detector was modeled with an MCNP6 Monte Carlo simulation [22] and determined to be 0.84 ± 0.02 for an incident γ-ray beam energy of 15.0 MeV and a threshold setting of 1.35 MeV. Due to the high efficiency of the HPGe detector, the intensity of the γ-ray beam had to be attenuated to perform the paddle calibration measurements. The beam intensity was reduced using copper attenuators located upstream of the beam-shaping collimator [20]. First, the paddle was used to measure the flux of an unattenuated beam. Next, the flux of the attenuated beam was measured with the HPGe detector positioned at 0° (directly in the beam path). The attenuation was calculated using the narrow beam attenuation coefficient for natural copper from the NIST database [23]. This factor was used to compute the flux of the unattenuated beam. The relative γ-ray beam flux upstream of the attenuators was monitored during the calibration runs (attenuated and not attenuated) using a radiation monitor located beside the γ-ray beam tube, just beyond the cavity mirror. The paddle efficiency was computed as the ratio of the paddle counting rate to the unattenuated beam flux (γ/s). This process was repeated for a 16.0-MeV beam.

The average efficiency of the paddle over the two calibration runs was determined to be $\epsilon_{\text{pad}} = 4.54 \times 10^{-4} \pm 3.2 \times$

TABLE I. Neutron detector geometry: The distances and angles are for center-to-center positions of the target and detectors.

Detector	Distance from Target (cm)	θ	ϕ
1	55.3 ± 0.2	90°	180°
2	55.6 ± 0.2	90°	270°
3	52.8 ± 0.2	135°	0°

10^{-5}. The sources of this error were the uncertainty in the efficiency of the HPGe detector, the integration of the counts in the energy spectrum of the detector, and the standard deviation in the average of the calibration runs, all added in quadrature. The standard deviation in the measurements of the paddle efficiency at 15.0 and 16.0 MeV was $\pm 4\%$. Due to the mild energy dependence of the photon mass attenuation coefficient for plastic scintillators in the energy range of the measurements [23], the paddle efficiency at the three energies of the experiment is expected to differ by less than $\pm 5\%$. The standard deviation of the calibration measurements is consistent with the theoretical predictions. The average paddle efficiency is therefore used for cross-section calculations at all three beam energies.

The selenium target consisted of 2.99 g of 99.45% isotopic-enriched ^{80}Se powder, encased in a plastic cylinder. The front and back ends of the plastic cylinder were 1.5 mm thick each, and the surrounding circular wall was 5.5 mm thick. The volume containing the ^{80}Se powder was 20-mm diameter $\times$ 5-mm long. Both dimensions were measured to a precision of ± 0.5 mm. The target was placed in the beam path, with the cylinder coaxial to the beam. The background due to (γ, n) reactions in the sample holder materials was measured using an identical empty plastic container. The empty-holder data were subtracted from the sample-in data to obtain the net (γ, n) events.

At each of the three beam energies, neutrons were measured with detectors placed at three angles, as shown in Figs. 3 and 4 and summarized in Table I. The quantity "Distance from Target" in Table I is the center-to-center distance between the target and the detector. The detector distances were measured to a precision of ± 2 mm. The angles θ and ϕ define the direction from the center of the target to the center of each detector, with θ denoting the scattering angle and ϕ denoting the azimuthal angle. Detectors 1 and 2 were each placed at a scattering angle of $\theta = 90°$, and Detector 3 was at a scattering angle of $\theta = 135°$. Detector 2 was positioned at an azimuthal angle of $\phi = 270°$. Detectors 1 and 3 were each positioned in the horizontal plane (same as the beam polarization) on opposite sides of the beam axis.

The front of each detector was covered with a 2.4 mm-thick lead disk to desensitize the liquid scintillators to the prompt γ-ray flash due to Compton scattering of the incident γ-ray beam bunch off the atomic electrons in the target. The γ-ray background was further reduced by applying pulse-shape analysis. The hardware pulse-height thresholds on the neutron detectors were set to 30 keVee to allow analysis of the data at a software threshold (PH cut) of 59 keVee. The detector software threshold setting was determined using the γ-rays
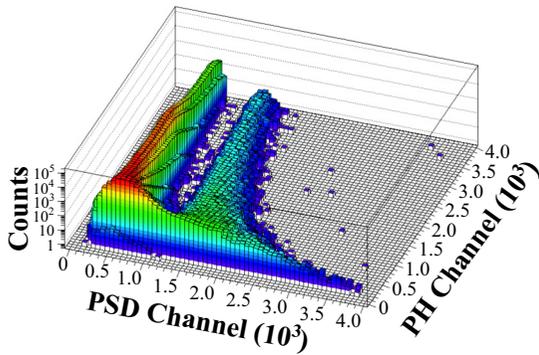
FIG. 5. 2D Histogram of the detector pulse shape (PSD, x axis) vs. pulse height (PH, y axis) for counts in Detector 1 from the ^{80}Se(γ, n) reaction at incident beam energy of $E_\gamma = 15.6$ MeV. The sharp distribution of counts centered around channel 500 on the PSD axis is due to γ rays that come mostly from Compton scattering of the incident beam off electrons in the ^{80}Se sample and the sample holder. The distribution centered around channel 1500 is due to neutrons and represents the data. The data analysis rejected counts with PSD channels less than 1050 and PH channels less than 354 (59 keVee).

from ^{241}Am. A two-dimensional (2D) histogram of pulse shape (average decay times) versus pulse height is shown in Fig. 5. The distribution with the longer decay times represents the events in the detector due to neutrons. The pulse-shape discrimination (PSD) cut was set to reject signals with decay times less than channel 1050. The technique of γ rejection by PSD is illustrated in Fig. 6 by the overlay of a TOF spectrum with only a PH threshold cut against a TOF spectrum with both PH and PSD cuts. At the threshold of the analysis (59 keVee), 98% of the counts due to γ rays were rejected by the PSD cut.

An example of a TOF histogram measured at $E_\gamma = 15.6$ MeV is shown in Fig. 7 for data collected with the ^{80}Se target in the beam (unshaded curve) and for an empty holder (shaded curve). Notice the high signal-to-background ratio in the region of the neutron spectrum. The PSD and PH
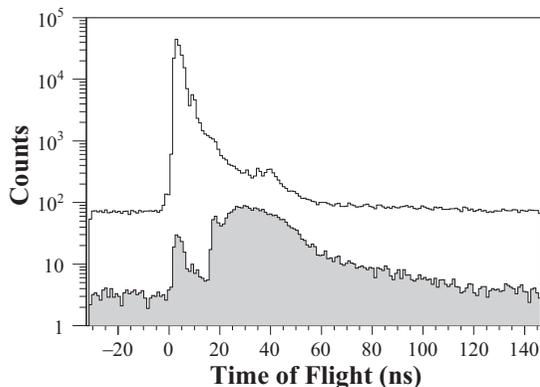

FIG. 6. Particle time-of-flight (TOF) histograms analyzed under two conditions: (i) with a 59-keVee PH cut (unshaded). (ii) With both a 59-keVee PH cut and a PSD cut to reject counts with PSD channel less than 1050 (shaded). These data were collected by Detector 1 ($\theta = 90°$, $\phi = 180°$) with incident beam energy $E_\gamma = 15.6$ MeV.
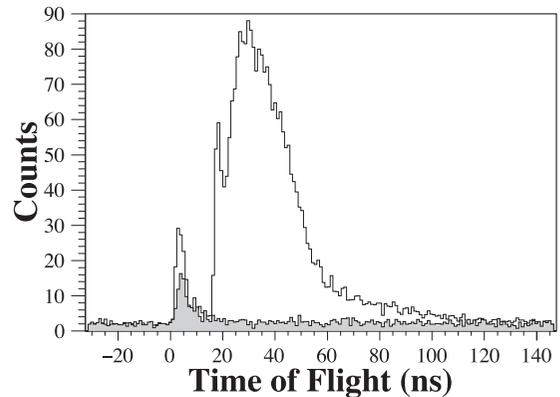

FIG. 7. Plots of neutron TOF histograms for sample-in (unshaded) and empty-holder (shaded) runs at incident beam energy $E_\gamma = 15.6$ MeV. These data were collected with Detector 1 ($\theta = 90°$ and $\phi = 180°$). A 59-keVee PH cut and a PSD cut at channel 1050 have been imposed (see Figs. 5 and 6). The enhancement around 4 ns is the remainder of the γ flash that survives the PSD cut. The part of the neutron TOF spectrum that was examined is from around 16 ns to around 52 ns. The enhancement around 17 ns is only observed by Detector 1 and is believed to be due to the distribution of neutrons with orbital angular momentum of $\ell = 1$.

cuts have been applied to both histograms. The empty-holder background histogram was normalized to the histogram accumulated with the target in the beam using the relative paddle counts. The net neutron TOF histogram for the ^{80}Se(γ, n) reaction was generated by subtracting the background histogram from the target histogram. The neutron energy histogram shown in Fig. 8 was computed from the TOF spectrum in Fig. 7.
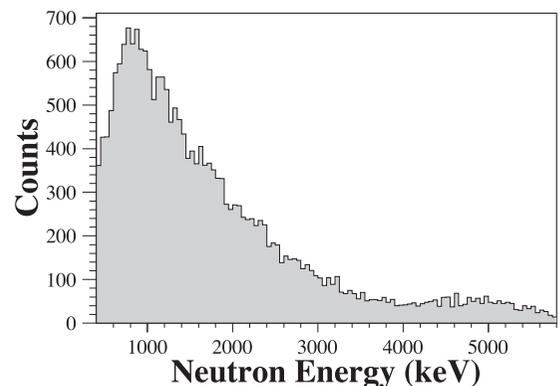

FIG. 8. Plot of the histogram of the energy of the detected neutrons at incident beam energy $E_\gamma = 15.6$ MeV. These data were collected with Detector 1 ($\theta = 90°$ and $\phi = 180°$). A 59-keVee PH cut and a PSD cut at channel 1050 have been imposed (see Figs. 5 and 6). The background obtained from the empty-holder run has been subtracted from the spectrum obtained from the sample-in run. Detector efficiency and neutron effective transmission were not compensated for in this histogram, so the sharp drop-off at energies below around 800 keV due to decreasing detector efficiency is clearly visible.

III. DATA ANALYSIS AND RESULTS

The main objective of the analysis was to determine the differential cross sections for the ^{80}Se$(\gamma, n)^{79}$Se reaction as a function of the excitation energy in the residual ^{79}Se nucleus. Cross sections were measured for three incident γ-ray beam energies: 15.6 MeV, 15.8 MeV, and 16.0 MeV. These measured cross sections will be compared to statistical model calculations in Sec. IV to determine the parameters of the nuclear level density for low-spin states in ^{79}Se that best describe the data. The three main steps in the data analysis were: (i) to determine the angle-correlated differential cross sections for each incident beam energy from the counts in the neutron TOF spectrum measured at three detector angles, (ii) to simultaneously fit the three angle-correlated differential cross sections at each beam energy in order to determine the matrix elements as a function of excitation energy in the formalism by Weller *et al.* [12,13] for (γ, particle) nuclear reactions, and (iii) to integrate the differential cross sections over a solid angle of 4π, using the matrix elements determined at every excitation energy, to obtain the (γ, n) excitation energy spectrum (i.e., the angle-integrated differential cross section). The details of each step are described in this section.

A. Determination of cross sections from detector counts

The angle-correlated differential cross section for the ^{80}Se(γ, n) reaction was computed from the measured neutron energy spectrum using:

$$\frac{d\sigma(E_n, \theta, \phi)}{dE_n d\Omega} = \frac{N(E_n, \theta, \phi)}{N_\gamma \beta \rho_N \epsilon(E_n) \alpha(E_n) dE_n d\Omega}, \quad (1)$$

where $N(E_n, \theta, \phi)$ is the neutron energy (E_n) spectrum (counts/keV) measured at detector angles (θ, ϕ), N_γ is the number of γ's incident on the target, β is the transmission fraction of incident beam photons calculated at the center of the target, ρ_N is the nuclear density of the ^{80}Se target (6.76×10^{21} nuclei/cm^2), $\epsilon(E_n)$ is the detector efficiency for neutrons with energy E_n, $\alpha(E_n)$ is the effective transmission of neutrons along the path from the reaction site in the target to the detector, dE_n is the width of the bins (keV) in the neutron energy spectra, and $d\Omega$ is the solid angle of the neutron detector (steradians).

The number of γ's incident on the target was measured with the thin plastic scintillator paddle that was located upstream. This quantity is given by:

$$N_\gamma = \frac{N_\mathrm{pad}}{\epsilon_\mathrm{pad}}, \quad (2)$$

where N_pad is the number of counts registered by the paddle during the acquisition of the neutron energy spectrum and ϵ_pad is the γ-ray detection efficiency of the paddle, cross calibrated against that of an HPGe detector.

The γ rays incident on the target sample were subject to attenuation from the plastic holder and the selenium in the target. The effective transmission β of γ rays in the sample was calculated using the narrow beam attenuation coefficients for selenium and lucite from the NIST database [23] and was determined to be 0.982.

TABLE II. Sources of systematic uncertainty in the differential cross-section measurement.

Source	% Error
Paddle Efficiency (ϵ_pad)	$\pm 7\%$
Neutron Detector Efficiency (ϵ_D)	$\pm 4\%$
Neutron Effective Transmission (α)	$\pm 5\%$
Total Systematic Uncertainty	$\pm 10\%$

The sources and magnitudes of statistical and systematic uncertainties are described below. The error bars on the data represent only the statistical uncertainties. The statistical uncertainty in the differential cross section was primarily due to the counting uncertainty in $N(E_n, \theta, \phi)$ in Eq. (1) (i.e., the statistical uncertainty in N_γ was negligible). It was calculated using:

$$\Delta\sigma = \Delta N = \sqrt{N_F + p^2 N_B}, \quad (3)$$

where N_F is the number of counts in the sample-in spectrum, N_B is the number of counts in the empty-holder spectrum, and p is the ratio of the paddle counts for the foreground measurements to that for the background measurements. The statistical uncertainty in p was negligible.

There were three major sources of systematic uncertainty in the differential cross-section measurements: the error in the incident beam flux measurement (relies on the paddle efficiency), the uncertainty in the detection efficiency of the liquid scintillators, and the uncertainty in the effective transmission of neutrons along the flight path from the target to the detectors. These uncertainties are summarized in Table II. The total relative systematic uncertainty in the cross-section data was estimated to be $\pm 10\%$.

The efficiency of the liquid scintillators was simulated using Monte Carlo codes NRESP7 and NEFF7, developed by Dietze and Klein at Physikalisch-Technische Bundesanstalt (PTB) [24]. This code has been demonstrated to reproduce the shape of the efficiency curve as a function of neutron energy with a precision better than $\pm 2\%$ and an absolute efficiency with an uncertainty of $\pm 4\%$. The data were analyzed with a detector threshold setting of 59 keVee. The efficiency curve for a 59-keVee threshold is shown in Fig. 9.

The excitation energy of the residual nucleus is related to the energy of the emitted neutrons by conservation of energy:

$$E_x = E_\gamma - S_n - E_n, \quad (4)$$

where E_x is the excitation energy in the residual ^{79}Se nucleus, E_γ is the energy of the incident γ-ray beam, S_n is the neutron separation energy of ^{80}Se (9.9 MeV), and E_n is the kinetic energy of the emitted neutron. By this relationship, the energy threshold for neutron detection determines the maximum excitation energy that can be probed in the residual nucleus for a specific E_γ. With a threshold setting of 59 keVee, the detectors were sensitive to neutrons down to about 250 keV. However, data are reported for neutron energies greater than 600 keV, which is about 80% up the initial steep rise in the detector efficiency as a function of neutron energy (see Fig. 9).
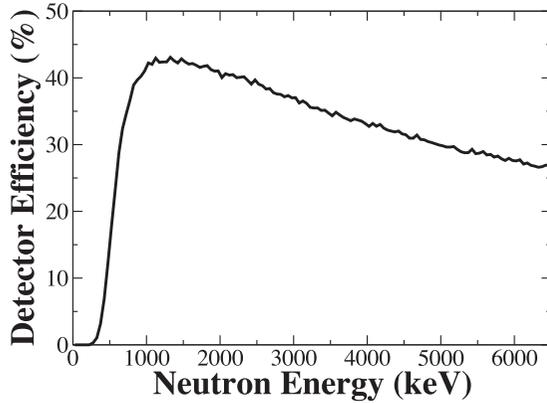
FIG. 9. Plot of the neutron detector efficiency for the 2-in. diameter × 2-in. thick liquid scintillators used in these measurements. These calculations were performed for a 59-keVee PH threshold using the PTB computer code [24].
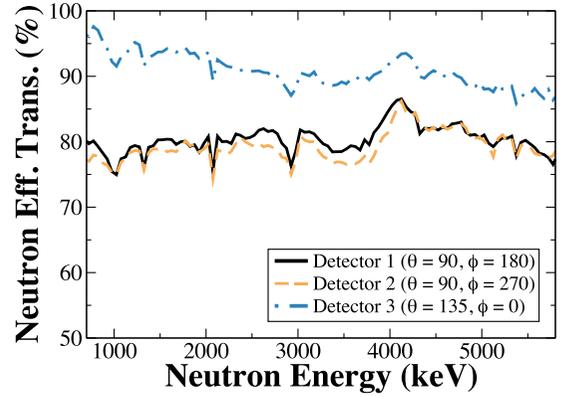

FIG. 10. Plots of the effective transmission of neutrons from the target to each detector as a function of neutron energy. These calculations were made for an incident beam energy of 15.6 MeV. An MCNP6 Monte Carlo simulation [22] transported the neutrons outward to the detectors from the location of the reaction in the target. The simulation tracked both neutron out-scattering and in-scattering. The neutron interactions were computed using cross sections from the ENDF/B-VII.1 database [25].

The emitted neutrons can scatter off the nuclei in the target, off the plastic sample holder that surrounds the target, and in other materials between the target and the detector (i.e., the beam pipe holding the target container, the air between the target and detector, and the lead shielding on the detector face). The scatter effects were computed with an MCNP6 simulation [22] that tracked the neutrons along their trajectories from the point of origin in the target to the neutron detector. The simulation accounted for contributions to the neutron energy spectrum due to out-scattering (i.e., neutrons that were emitted in directions that fell within the solid angle of the detector but were scattered to directions that miss the detector) and in-scattering (i.e., neutrons that were emitted in directions that fell outside the solid angle of the detector but were scattered to directions that intersect the detector). Out-scattering is the effect more commonly referred to as attenuation. The simulation also included loss of neutrons from neutron-induced reactions [e.g., (n, p), (n, α), and (n, γ)]. The effective transmission $\alpha(E_n)$ is determined by subtracting these effects (attenuation, in-scattering, and reactions). Plots of $\alpha(E_n)$ for neutrons incident on the three detectors are shown in Fig. 10. The neutron scattering and reaction cross sections used in the simulations are taken from the ENDF/B-VII.1 evaluated database [25]. The systematic error in the computed value of $\alpha(E_n)$ was estimated to be ±5% and was obtained by adding in quadrature the uncertainties in the cross sections of the scattering processes encountered along the flight path.

The measured angle-correlated differential cross sections for the ^{80}Se$(\gamma, n)^{79}$Se reaction are shown in Figs. 11(a), 12(a), and 13(a). The observed exponential growth of the differential cross section as a function of excitation energy (E_x) reflects the nuclear level density of low-spin states in ^{79}Se: the number of allowed nucleon configurations in the residual nucleus increases exponentially with increasing excitation energy. The curves that are overlaid with the data in the three figures are calculations from fits to the data using the angular correlation formalism of Weller *et al.* [12,13]. The curve in each panel (a) is the fit to the cross-section data measured with Detector 1.

B. Determination of reaction matrix elements

The angle-correlated differential cross-section data were fit using the formalism by Weller *et al.* [12,13] to determine the reaction reduced matrix elements as a function of excitation energy. A graphical representation of the steps in the (γ, n) reaction is shown in Fig. 1. In the first step, the incident γ ray is absorbed by the ^{80}Se nucleus, inducing an electric dipole $(E1)$ transition from the 0^+ ground state to an excited state with spin and parity $J^\pi = 1^-$ and excitation energy equal to the energy of the absorbed γ ray. Next, the excited 1^- state in ^{80}Se decays to ^{79}Se by emission of a neutron. This decay can be directly to the ground state of ^{79}Se, which would result in the maximum kinetic energy of the emitted neutron, or to an excited state, as indicated by the arrows in Fig. 1. The excited ^{79}Se nucleus then relaxes to the ground state by emission of γ rays. By conservation of total angular momentum:

$$\vec{J}_{^{80}\mathrm{Se}^*} = \vec{J}_{^{79}\mathrm{Se}} + \vec{\mathcal{S}}_n + \vec{\ell}_n, \qquad (5)$$

where $J_{^{80}\mathrm{Se}^*}$ is the total angular momentum of the excited state in ^{80}Se, $J_{^{79}\mathrm{Se}}$ is the total angular momentum of the residual state in ^{79}Se, $\mathcal{S}_n$ is the intrinsic spin of the neutron (1/2), and ℓ_n is the orbital angular momentum of the neutron.

The expression for the angular distribution of the differential cross section of the (γ, n) reaction induced with linearly polarized γ rays is given in terms of reduced matrix elements $(R_t$ and $R'_t)$ by Refs. [12,13]:

$$\sigma(\theta, \phi) = \frac{\lambdabar^2}{6} \Sigma_{tt'k'} \left[\left(B_{0\,0}^{k'0} + \frac{1}{\sqrt{10}} B_{2\,0}^{k'0} \right) R_t R'_{t'} P_{k'}(\cos\theta) \right.$$

$$\left. - f\sqrt{\frac{3}{5}} \cos(2\phi) B_{2\,2}^{k'2} R_t R'_{t'} P_{k'}^2(\cos\theta) \right], \qquad (6)$$

where $\lambdabar$ is the reduced wavelength, f is the polarization fraction $(f = 1$ for linear polarization), $P_{k'}$ are Legendre polynomials $(k' = 0$ or 2 for linear polarization), and $B_{k\,q}^{k'q'}$

are angular correlation coefficients that were computed as prescribed by Weller *et al.* [12,13].

The subscripts t and t' indicate summation over p, L, b, ℓ, and s in the incident (t) and exit (t') channels: p is the the electromagnetic (EM) mode of the γ-ray resonance [$p = 0$ (for magnetic) or 1 (for electric)], L is the multipolarity of the incident photons, b is the total angular momentum of the system ($b = J_{^{80}\text{Se*}}$), ℓ is the orbital angular momentum of the outgoing neutron, and s is the channel spin.

The summation includes all possible EM modes and all possible angular momenta. Some simplifying assumptions were made to limit the number of terms in the summation. At the γ-ray beam energies of the measurements, the giant dipole resonance (GDR) is the dominant collective response of the ^{80}Se nucleus ($p = 1$, $L = 1$, $b = 1$). The value of ℓ was limited to 0 or 1, an assumption that is supported by the quality of the fits. The channel spin s is given by the vector sum:

$$\vec{s} = \vec{J}_{^{79}\text{Se}} + \vec{\tfrac{1}{2}}. \tag{7}$$

This leads to the following relationships:

$$\vec{b} = \vec{\ell} + \vec{s} \tag{8}$$

and

$$\vec{k}' = \vec{b} + \vec{b}'. \tag{9}$$

By conservation of total angular momentum, $s = 1$ for $\ell = 0$, and $s = 0$, 1, or 2 for $\ell = 1$. Because the strong nuclear and electromagnetic interactions conserve parity, the parity of the states in ^{79}Se is determined by the orbital angular momentum of the emitted neutron. The corresponding angular momenta and parities of the states populated in ^{79}Se are $J^{\pi}_{^{79}\text{Se}} = 1/2^-$ or $3/2^-$ (for $\ell = 0$) and $J^{\pi}_{^{79}\text{Se}} = 1/2^+$, $3/2^+$, or $5/2^+$ (for $\ell = 1$). Based on the simplifying assumptions and conservation of angular momentum, p, L, and b are constants over the summation in Eq. (6). Thus, the t (t') index is reduced to ℓ and s (ℓ' and s'). Also, because a pure $E1$ transition in ^{80}Se was assumed, there are no interference terms in the products of the reduced matrix elements ($R_{\ell s} = R'_{\ell' s'}$), which leads to $R_{\ell s} R'_{\ell' s'} = R_{\ell s}{}^2$.

The cross section is a superposition of the neutrons emitted with $\ell = 0$ and $\ell = 1$:

$$\sigma = \sigma_{\ell=0} + \sigma_{\ell=1}. \tag{10}$$

The angular-momentum decomposed cross sections can be written as the incoherent sums of the (γ, n) reaction cross sections for leaving ^{79}Se in the corresponding J^{π} states:

$$\sigma_{\ell=0} = \sigma\left(\tfrac{1}{2}^-\right) + \sigma\left(\tfrac{3}{2}^-\right) \tag{11}$$

and

$$\sigma_{\ell=1} = \sigma\left(\tfrac{1}{2}^+\right) + \sigma\left(\tfrac{3}{2}^+\right) + \sigma\left(\tfrac{5}{2}^+\right). \tag{12}$$

Applying all of these constraints to Eq. (6), the expression for the cross-section angular distribution becomes:

$$\sigma(\theta, \phi)_{^{80}\text{Se}(\gamma,n)} = \frac{\lambdabar^2}{6}\Big[4.50 R_{01}{}^2 + \big[2.25 - 2.25 P_2(\cos\theta) + 1.125 P_2^2(\cos\theta)(\cos 2\phi)\big]R_{10}{}^2 + \big[4.50 + 2.25 P_2(\cos\theta)$$

$$- 1.125 P_2^2(\cos\theta)(\cos 2\phi)\big]R_{11}{}^2$$

$$+ \big[4.50 - 0.450 P_2(\cos\theta)$$

$$+ 0.225 P_2^2(\cos\theta)\cos(2\phi)\big]R_{12}{}^2\Big]. \tag{13}$$

As stated above, for the imposed constraint on the orbital angular momentum of the neutron ($\ell = 0$ or 1), the residual ^{79}Se nucleus will be produced in one of five states. This simplified expression for the differential cross section depends only on four reduced matrix elements: R_{01}, R_{10}, R_{11}, and R_{12} [see Eq. (13)].

The Legendre polynomials in Eq. (13) were evaluated for the angles of the three neutron detectors to give expressions for the angle-correlated differential cross sections measured by each detector in terms of the pertinent $R_{\ell s}$ values:

$$\sigma_1(90°, 180°) = \frac{\lambdabar^2}{6}\big[4.5 R_{01}{}^2 + 6.75 R_{10}{}^2 + 5.4 R_{12}{}^2\big], \tag{14}$$

$$\sigma_2(90°, 270°) = \frac{\lambdabar^2}{6}\big[4.5 R_{01}{}^2 + 6.75 R_{11}{}^2 + 4.05 R_{12}{}^2\big], \tag{15}$$

and

$$\sigma_3(135°, 0°) = \frac{\lambdabar^2}{6}\big[4.5 R_{01}{}^2 + 3.375 R_{10}{}^2 + 3.375 R_{11}{}^2 + 4.725 R_{12}{}^2\big]. \tag{16}$$

To better illustrate the anisotropy of the angular distribution, asymmetries were computed from the angle-correlated cross sections. The asymmetry is a measure of the fractional difference between the differential cross sections measured at two different angles. Using the differential cross-section data measured at three detector angles (σ_1, σ_2, and σ_3), the azimuthal asymmetry (Σ_{12}) between Detectors 1 and 2 and the scattering asymmetry (Σ_{13}) between Detectors 1 and 3 were computed. These asymmetries are given by:

$$\Sigma_{12}(E) = \frac{\frac{d\sigma_1(90°,180°,E)}{dEd\Omega} - \frac{d\sigma_2(90°,270°,E)}{dEd\Omega}}{\frac{d\sigma_1(90°,180°,E)}{dEd\Omega} + \frac{d\sigma_2(90°,270°,E)}{dEd\Omega}} \tag{17}$$

$$\Sigma_{13}(E) = \frac{\frac{d\sigma_1(90°,180°,E)}{dEd\Omega} - \frac{d\sigma_3(135°,0°,E)}{dEd\Omega}}{\frac{d\sigma_1(90°,180°,E)}{dEd\Omega} + \frac{d\sigma_3(135°,0°,E)}{dEd\Omega}}. \tag{18}$$

The derived asymmetry data are plotted in Figs. 11(b) and 11(c) through 13(b) and 13(c) as functions of the excitation energy (E_x) in ^{79}Se. The curves in panels (b) and (c) are the fits to the respective angular asymmetries. Most of the systematic errors in the cross-section measurements cancel in the calculation of asymmetry. Error bars in the asymmetry plots represent only statistical uncertainties. The statistical uncertainties of the asymmetry calculations were computed using:

$$\Delta\Sigma_{12} = \frac{\sqrt{4\sigma_2{}^2\Delta\sigma_1{}^2 + 4\sigma_1{}^2\Delta\sigma_2{}^2}}{(\sigma_1 + \sigma_2)^2} \tag{19}$$

and

$$\Delta\Sigma_{13} = \frac{\sqrt{4\sigma_3{}^2\Delta\sigma_1{}^2 + 4\sigma_1{}^2\Delta\sigma_3{}^2}}{(\sigma_1 + \sigma_3)^2}. \tag{20}$$
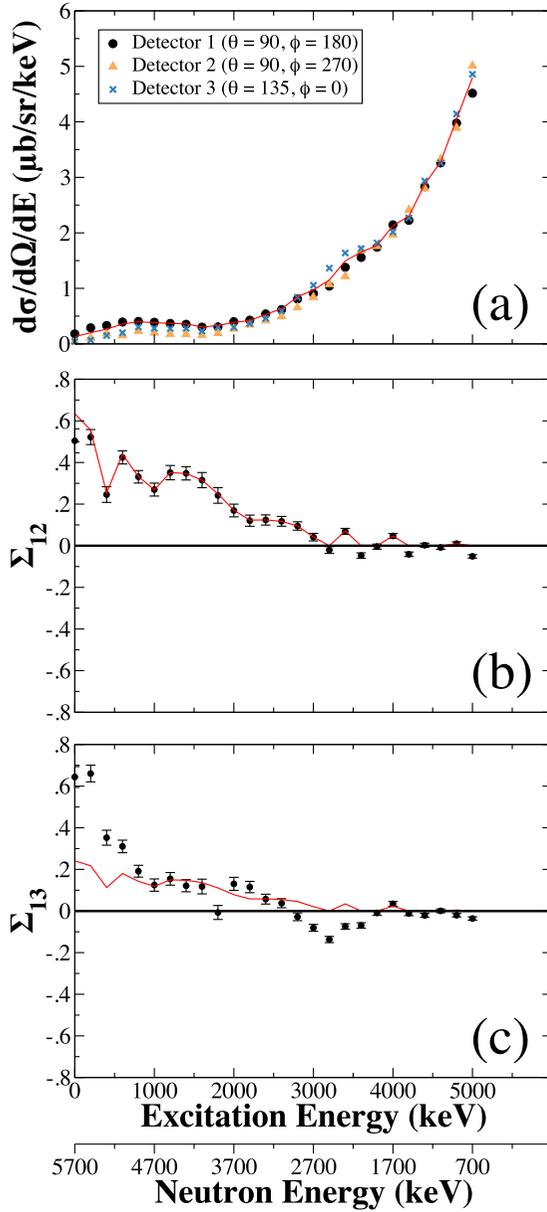
FIG. 11. Measured angle-correlated differential cross sections and asymmetries for the ^{80}Se(γ, n) reaction at incident γ-ray beam energy $E_\gamma = 15.6$ MeV. Measurements are reported both in terms of residual excitation energy (E_x) and neutron energy (E_n). (a) Overlay of plots of the differential cross sections at the three detector angles. (b) Azimuthal asymmetry of the cross sections measured at $\theta = 90°$. (c) Asymmetry in the cross sections measured at $\theta = 90°$ and $\theta = 135°$. The curves that are overlaid with the data are calculations from fits to the data using the angular correlation formalism of Weller *et al.* [12,13]. Error bars on the data represent statistical uncertainties only. Error bars in (a) are smaller than the size of the symbols.

The terms σ_N here refer to the angle-correlated differential cross sections $d\sigma_N/dEd\Omega$.

The data were fit with Eqs. (14)–(16) for the angle-correlated differential cross sections to determine the four $R_{\ell s}$ matrix values as a function of excitation energy. The χ^2 fitting algorithm was applied independently for each excita-
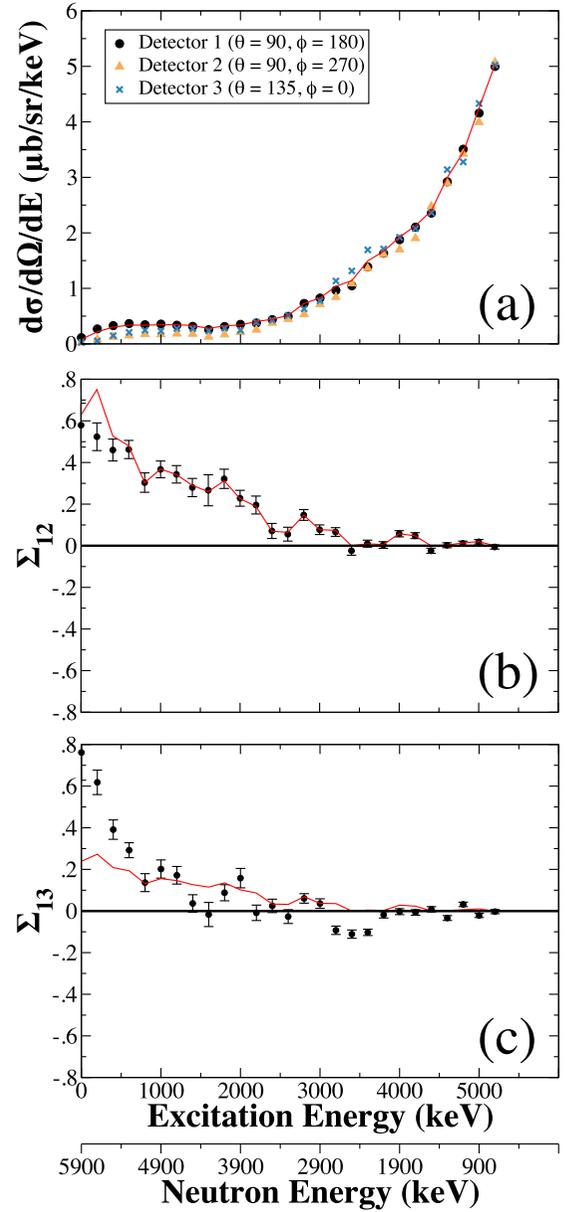
FIG. 12. Measured angle-correlated differential cross sections and asymmetries for the ^{80}Se(γ, n) reaction at incident γ-ray beam energy $E_\gamma = 15.8$ MeV. The data and curves are as described in Fig. 11.

tion energy bin. Also, the data sets for each incident beam energy were fit independently. The data at each excitation energy were fit by searching for the values of R_{01}, R_{10}, R_{11}, and R_{12} that minimized the total χ^2 value in the comparison of the calculated and measured cross sections. The R_{01} term represents the s-wave ($\ell = 0$) contribution to the reaction, which results in the decay to states in ^{79}Se with J^π equal to $1/2^-$ or $3/2^-$. The R_{10}, R_{11}, and R_{12} terms represent the p-wave ($\ell = 1$) contributions to the reaction, which produce decays to states in ^{79}Se with J^π equal to $1/2^+$, $3/2^+$, or $5/2^+$. The R_{10} matrix element accounts completely for the cross section for decay to $1/2^+$ states. The cross sections for decay
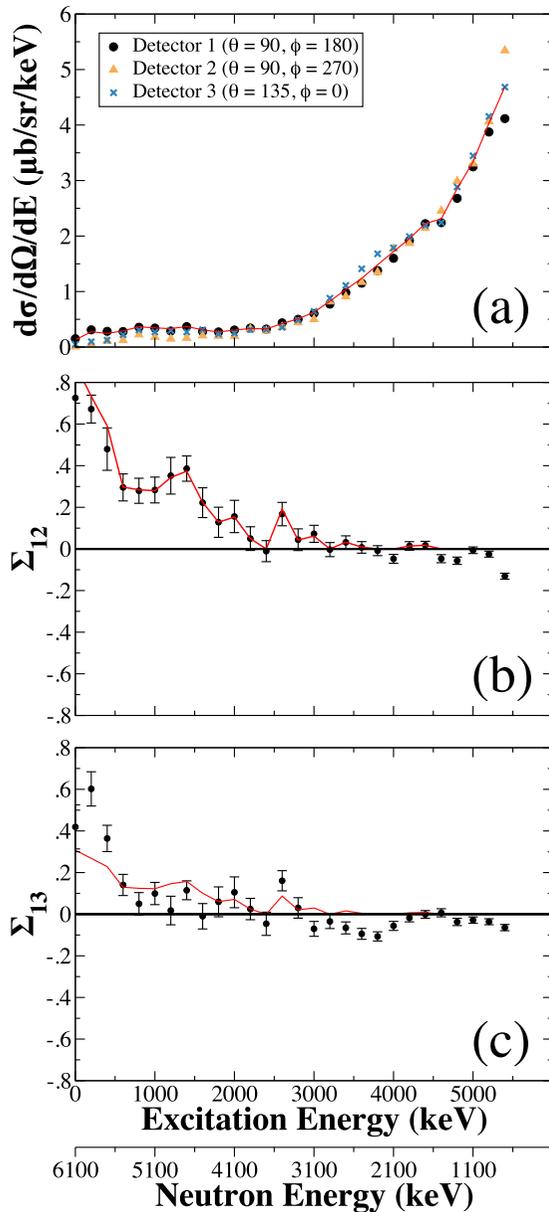
FIG. 13. Measured angle-correlated differential cross sections and asymmetries for the ^{80}Se(γ, n) reaction at incident γ-ray beam energy $E_\gamma = 16.0$ MeV. The data and curves are as described in Fig. 11.

FIG. 14. Plots of the total χ^2 value for fits to our data. Values are reported both in terms of residual excitation energy (E_x) and neutron energy (E_n). These data were calculated for an incident γ-ray beam energy of 15.6 MeV, using different combinations of the reduced matrix elements $(R_{\ell s})$ in the expression for the angle-correlated cross section derived by Weller *et al.* [12,13]. The fits constrained the orbital angular momentum of the detected neutrons to be $\ell = 0$ or 1. Comparisons of the χ^2 plots indicate that including R_{11} and R_{12} does not significantly improve the quality of the fit to the data; the data are most sensitive to the values of R_{01} and R_{10}.

to $3/2^+$ and $5/2^+$ states are due to the combination of the R_{11} and R_{12} elements.

Good fits to the data were achieved using only the R_{01} and R_{10} matrix elements. Including the R_{11} and R_{12} did not improve the quality of the fits by a statistically significant amount, as assessed by the change in the χ^2 values shown in Fig. 14. The value of R_{01} determines the magnitude of the portion of the cross section that is isotropic in angle. Therefore, changing this parameter in the fit does not change the calculated asymmetry. Increasing the value of R_{10} increases the calculated value of the differential cross section at the angle of Detector 1 to a greater degree than those at the angles
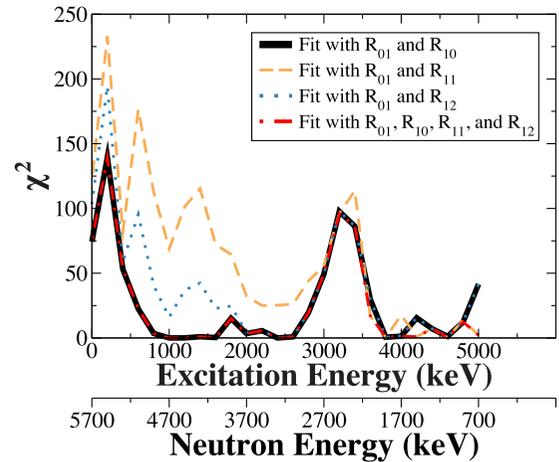
of Detectors 2 and 3, thereby making both Σ_{12} and Σ_{13} more positive. The change to Σ_{13} is less than that to Σ_{12}. Increasing the value of R_{11} produces a negative Σ_{12} asymmetry, which differs from the data, thereby indicating that the value of this matrix element must be small. The value of R_{12} has only a minor impact on the calculated asymmetries. Given these observations, the simplifying assumption was made that the R_{11} and R_{12} matrix elements can be neglected in the data fits. This result suggests that the data are selectively sensitive to the structure of the $1/2^-$ and $3/2^-$ states in ^{79}Se via emission of s-wave neutrons and to the $1/2^+$ states via emission of p-wave neutrons. The values for R_{01} and R_{10} as a function of excitation energy, obtained by fitting the data for the three incident beam energies, are plotted in Fig. 15.

As illustrated in Figs. 11–13, the quality of the fit by the two parameter model to the Σ_{12} asymmetry is better than that to the Σ_{13} asymmetry. The quality of the fits to both the cross-section and asymmetry data are about the same at each incident γ-ray beam energy. The aggregate χ^2 values of the fit to the data for an incident beam energy of 15.6 MeV are given in Fig. 14. Both Σ_{12} and Σ_{13} are positive in the E_x range from 0 to about 2500 keV. However, the fit to Σ_{13} below E_x of about 900 keV is lower than the data. This discrepancy between the data and the fit is reflected in the rise in χ^2 values at neutron energies larger than 5000 keV (see Fig. 14). The Σ_{13} becomes negative with no corresponding feature in the Σ_{12} from about $E_x = 3300–3700$ keV, and the fit is unable to describe this feature. This difference between the fit and the Σ_{13} data causes the plateau in the χ^2 values at neutron energies between 2000 and 3000 keV. The model with only $\ell = 0$ or 1 matrix elements is not able to account for the rise
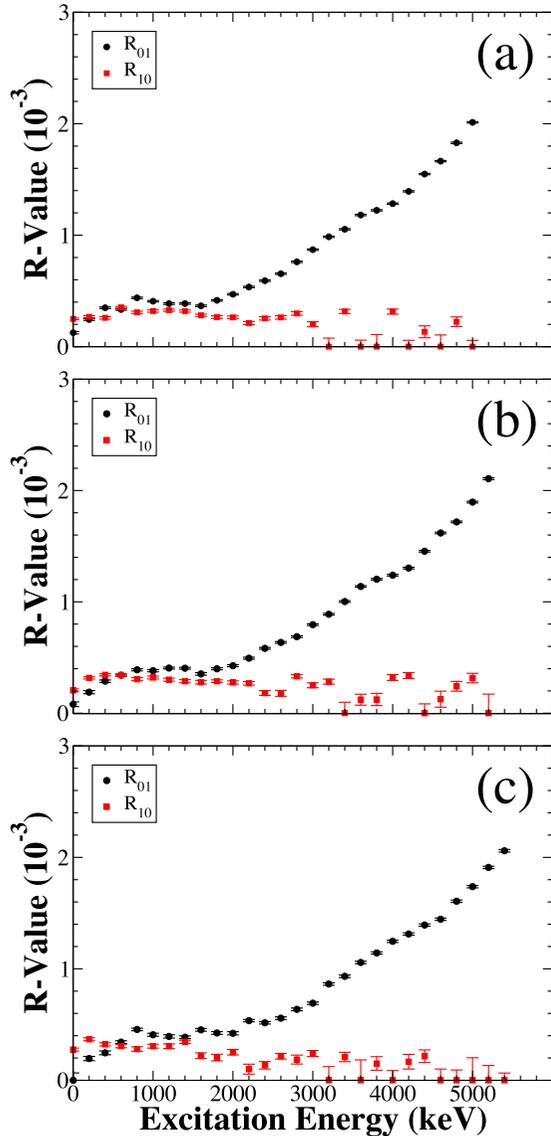
FIG. 15. The values of R_{01} and R_{10} obtained by fitting the differential cross-section data for the ^{80}Se(γ, n) reaction to the expression for the angle-correlated cross section derived by Weller *et al.* [12,13]. The fits constrained the orbital angular momentum of the detected neutrons to be $\ell = 0$ or 1. (a) R values for the data measured at $E_\gamma = 15.6$ MeV. (b) R values for the data measured at $E_\gamma = 15.8$ MeV. (c) R values for the data measured at $E_\gamma = 16.0$ MeV. Error bars represent uncertainty in the χ^2 fit.

in the value of Σ_{13} below E_x of 900 keV nor for the negative values of Σ_{13} between E_x of 3300 and 3700 keV. These discrepancies between the model fit and the data raise the possibility that a significant fraction of the neutrons emitted in these two energy ranges (from $E_n = 2000$–3000 keV and above $E_n = 5000$ keV) may have orbital angular momentum of $\ell = 2$ or greater.

C. Computation of excitation energy spectrum

The angle-integrated differential cross section (i.e., excitation energy spectrum) for the ^{80}Se$(\gamma, n)^{79}$Se reaction was
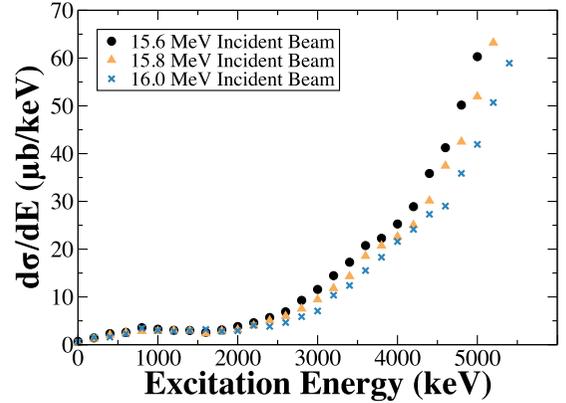

FIG. 16. Overlaid plot of the angle-integrated differential cross sections (excitation energy spectra) of the ^{80}Se(γ, n) reaction for the three incident γ-ray beam energies. Error bars representing the statistical uncertainties are smaller than the size of the symbols.

computed using the reduced matrix elements determined by fitting the angle-correlated differential cross-section data. To obtain this quantity, Eq. (13) was integrated over a solid angle of 4π (with the values of R_{11} and R_{12} equal to 0). The resulting expression for the angle-integrated differential cross section as a function of the excitation energy (E_x) in ^{79}Se is given by:

$$\frac{d\sigma(E_x)}{dE_x} = \frac{4\pi \hbar^2}{6} [4.5 R_{01}(E_x)^2 + 2.25 R_{10}(E_x)^2]. \quad (21)$$

This expression was evaluated by substituting into the function the values of $R_{01}(E_x)$ and $R_{10}(E_x)$ that were obtained by fitting the angle-correlated cross-section data as described above. The angle-integrated differential cross-section data obtained from the measurements at the three γ-ray beam energies are overlaid in Fig. 16. In the next section, the measured differential cross sections will be integrated over energy to estimate the total (γ, n) cross sections, and the measured excitation spectra will be compared to differential cross-section calculations from a Hauser-Feshbach statistical model [16,17] to extract information about the level density of low-spin states in ^{79}Se.

IV. COMPARISON OF DATA TO STATISTICAL MODEL CALCULATIONS

The ^{80}Se$(\gamma, n)^{79}$Se reaction at the excitation energies of these measurements is expected to be dominated by $E1$ γ-ray excitation, followed by the decay of the excited ^{80}Se compound nucleus by emission of a neutron. This reaction mechanism is favored over direct particle ejection because of the low kinetic energy of the neutrons. The probability for the 1^- excited state in ^{80}Se to decay by neutron emission into a particular state with excitation energy E_x and spin and parity J^π in ^{79}Se depends on the product of the nuclear level density in the ^{79}Se residual nucleus and the transmission coefficients for the neutron exit channel [26].

Our measurements provide the first data for the differential cross sections of the ^{80}Se$(\gamma, n)^{79}$Se reaction as a function of

E_x. These data probe the level density of low-spin states in ^{79}Se up to an excitation energy of about 6 MeV. Previous experiments counted the emitted neutrons in ^{3}He or BF$_3$ ionization detectors, which were embedded in a material to moderate the neutrons. These measurements provided little or no information about the energy spectrum of the emitted neutrons [5,14,15,27–29]. In this section, our data are compared to previously published measurements and to Hauser-Feshbach calculations.

A. Integration of excitation energy spectrum to obtain total cross section

To compare our data to previous measurements of the total (γ, n) reaction cross section, our angle-integrated differential cross-section data were integrated with respect to excitation energy. Due to the 600-keV energy threshold setting used for the neutron detectors, about 30% of the full excitation function was not measured. Therefore, our measured cross-section data must be extrapolated from the maximum excitation energy of the measurements to the theoretical maximum excitation energy ($E_x^{\max}$). For example, at the incident beam energy of 15.6 MeV, the maximum allowed excitation energy in the residual ^{79}Se nucleus is 5700 keV, where the kinetic energy of the neutron is 0 keV. The maximum excitation energy of the measurements at this beam energy is 5100 keV, where the energies of the observed neutrons are cut off by the 600-keV threshold of the detectors.

The extrapolation was performed by fitting our energy differential data with a function that describes the general shape of the data and is constrained near the upper limit of the excitation energy, where the cross section approaches zero due to the collapse of phase space. An exponential function is used for the unconstrained cross section (σ_0), convoluted with the threshold shape of photonuclear reactions as described by Utsunomiya *et al.* [10].

The empirical function is given by:

$$\sigma(E_x) = \sigma_0(E_x)[(E_\gamma - S_n - E_x)/S_n]^p, \qquad (22)$$

where σ_0 is the unconstrained cross section, E_γ is the energy of the incident γ-ray beam, S_n is the neutron separation energy of ^{80}Se (9.9 MeV), E_x is the excitation energy of the residual ^{79}Se nucleus, and p is equal to $\ell + 1/2$ ($\ell = 0$ is assumed to dominate at low neutron energies/high excitations).

The functional form of σ_0 was taken as:

$$\sigma_0(E_x) = ae^{bE_x} + c. \qquad (23)$$

The parameters a, b, and c were fit to the data using a χ^2 minimization program.

The cross-section data were integrated over energy in two steps. In the first step, the measured data were integrated from $E_x = 0$ keV up to $E_x = 4800$ keV for a 15.6-MeV beam, up to $E_x = 5000$ keV for a 15.8-MeV beam, and up to $E_x = 5200$ keV for a 16.0-MeV beam. In each case, the upper bound of the integration was $E_n = 900$ keV (just beyond the cutoff due to the neutron detector threshold). In the second step, the empirical fit function was used to extrapolate the cross section to $E_x^{\max}$. The measured total cross sections are overlaid with empirical fit functions in Fig. 17. Total (γ, n) reaction cross
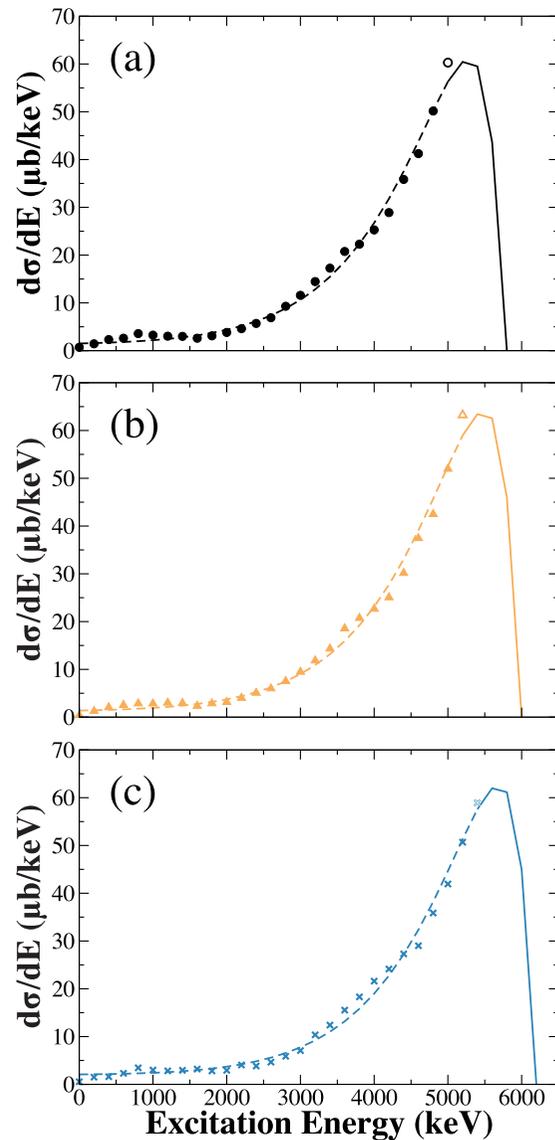

FIG. 17. Plots of the angle-integrated differential cross-section data overlaid with empirical fits used to integrate the excitation spectrum from $E_x = 0$ to $E_x^{\max}$ for (a) $E_\gamma = 15.6$ MeV, (b) $E_\gamma = 15.8$ MeV, and (c) $E_\gamma = 16.0$ MeV. The curves are solid in the extrapolated regions and dashed in the regions of observed data. The empty data points ($E_n = 700$ keV) are used to fit the empirical function but are excluded from the integration for the total cross section. Error bars representing the statistical uncertainties are smaller than the size of the symbols.

sections calculated using this method are reported in Table III, along with comparisons to measurements published by Carlos *et al.* and Goryachev *et al.* [14,15].

The uncertainty in the integral of the extrapolation function due to the statistical error in the fit is computed using the uncertainties of the three fit parameters (a, b, and c) in Eq. (23). The dispersions in the area underneath the extrapolated portion of the function are computed by raising and lowering the fit parameters by one standard deviation and reintegrating. These dispersions are added in quadrature to

TABLE III. Comparison of the total cross sections for the ^{80}Se$(\gamma, n)^{79}$Se reaction obtained in the present work to published values. Total experimental uncertainty in the measurements by Carlos *et al.* and Goryachev *et al.* was reported to be ± 7–8%.

Incident Beam Effective Centroid (MeV)	Total Cross Section Present Data (mb)	Carlos *et al.* [14] (1976) (mb)	Goryachev *et al.* [15] (1982) (mb)
15.6	108.7 ± 15.0	129.3 ± 9.1	132.2 ± 10.3
15.8	112.9 ± 16.1	134.6 ± 9.4	132.7 ± 10.9
16.0	113.1 ± 15.1	136.3 ± 9.5	128.1 ± 10.6

obtain the total uncertainty in the extrapolated integral. As an example, the fit to the data at 15.6 MeV is shown in Fig. 18. The values of the parameters for the best fit are denoted as a_0, b_0, and c_0. The one-σ errors in the fit parameters are Δa, Δb, and Δc, respectively. The uncertainties reported in Table III for our total (γ, n) cross section values reflect both the total systematic uncertainty of the differential cross-section measurements ($\pm 10\%$) and the extrapolation uncertainty, added in quadrature. The average uncertainty of the reported total (γ, n) cross sections is $\pm 14\%$.

The effective γ-beam centroids reported in Table III are computed using:

$$E_{\text{Cent.}} = \frac{\int E_\gamma \Phi(E_\gamma) \sigma(E_\gamma) dE_\gamma}{\int \Phi(E_\gamma) \sigma(E_\gamma) dE_\gamma}. \quad (24)$$

In this expression, E_γ is the γ-ray beam energy, $\Phi(E_\gamma)$ is the γ-ray beam energy profile (see Fig. 2), and $\sigma(E_\gamma)$ is an interpolated fit to the ^{80}Se(γ, n) cross sections reported by Carlos *et al.* and Goryachev *et al.* The results obtained from the two data sets were averaged. The function $\sigma(E_\gamma)$ shows little variance in the region of interest, and replacing it with a flat function had a negligible effect on the effective centroid calculation.

The total (γ, n) reaction cross sections obtained in the present work are 0.8–1.3 standard deviations smaller than those reported in the previous literature. One possible cause of this discrepancy would be if the method used to extrapolate our measurements down to zero neutron energy underestimates the total cross section by about 15%. If this is the case, then the steep rise in the cross section continues beyond the last measured point in the experiment, suggesting a substantially larger *s*-state level density at high excitation energies than that predicted by the Hauser-Feshbach calculations.

B. Fitting excitation energy spectrum with Hauser-Feshbach model for nuclear level density

The angle-integrated differential cross-section data were compared with Hauser-Feshbach calculations [30] performed using the code HF2002 by Grimes [31]. Input parameters included transmission coefficients and level-density parameters. The cross section was assumed to be entirely $E1$, and the corresponding entrance channel transmission coefficients were set to produce a total (γ, n) cross section of 117 mb. Transmission coefficients for protons and neutrons were taken from Koning and Delaroche [32] (global version), and those for α particles from McFadden and Satchler [33]. The bom-

barding energies used in the present measurements do not allow the emission of deuterons, tritons, or helium-3 particles.

A constant-temperature form for the level density with a nuclear temperature of 0.7 MeV gave the best fit to the shape of the cross-section excitation data. The parameters of the constant-temperature model are consistent with those found by von Egidy and Bucurescu [19] for medium mass nuclei. However, the fit diverges from the measured differential cross section at excitations above 5000 keV. Although modifications in the level-density parameters changed the relative neutron-to-proton and α-decay cross sections, the typical Hauser-Feshbach calculation already assigns the largest cross section to the neutron channel. These changes were therefore not large enough to match the measured data. However, the uncertainty in the calculated neutron transmission factor at high excitation energies (low neutron energies) may be larger than estimated. The differential cross sections calculated with the Hauser-Feshbach method are compared with the measured data in Fig. 19.
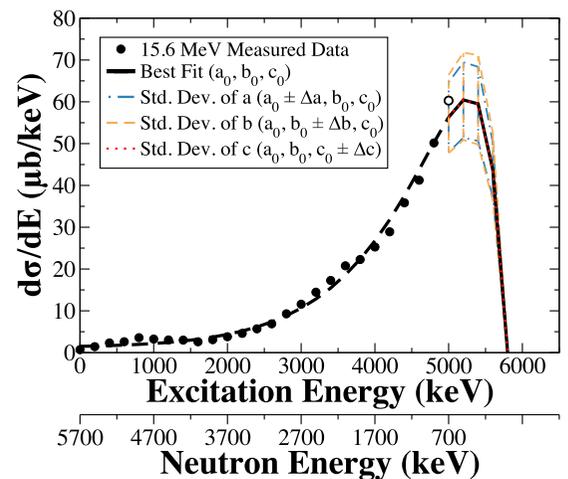

FIG. 18. Plot of the angle-integrated differential cross-section data for a 15.6 MeV incident beam energy overlaid with empirical fits made using Eq. (23). The bold black curve is made using the best-fit parameters (a_0, b_0, and c_0). This curve is solid in the extrapolated region ($E_x \geqslant 5000$ keV) and dashed in the region of observed data ($E_x \leqslant 4800$ keV). The curves above and below the bold black curve in the extrapolated region are calculated with the values of each of the three parameters separately varied by one standard deviation from the best fit. The empty circle data point ($E_n = 700$ keV) is used to fit the empirical function but is excluded from the integration for the total cross section.
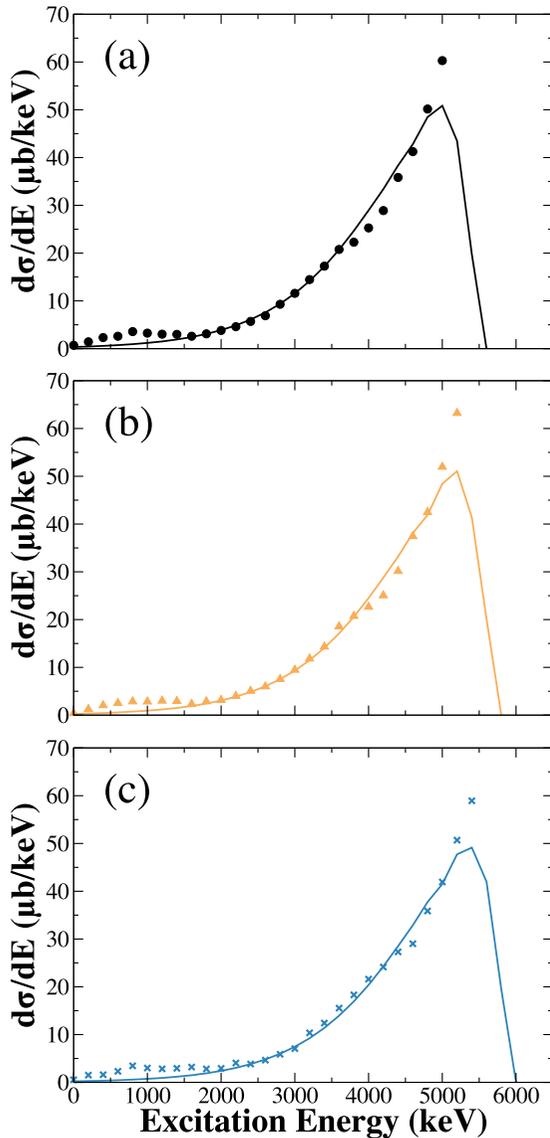
FIG. 19. Plots of the angle-integrated differential cross-section data compared to Hauser-Feshbach model calculations for (a) $E_\gamma =$ 15.6 MeV, (b) $E_\gamma =$ 15.8 MeV, and (c) $E_\gamma =$ 16.0 MeV. Error bars representing the statistical uncertainties are smaller than the size of the symbols.

Fermi-gas level-density parameters were obtained from Rohr [34], Al Quarishi *et al.* [35], Iljinov *et al.* [36], von Egidy and Bucurescu [19], and Goriely *et al.* [37]. None of these parameters yielded a fit with a χ^2 as low as that of the constant-temperature fit. This result is consistent with previous studies of nuclei in this mass region [19]. Some of the tested forms had a slope consistent with the energy dependence of the measured cross section, even though the magnitude was off. These forms had lower χ^2 than those with the wrong slope but a more consistent magnitude. The level densities are summarized in Table IV.

The Hauser-Feshbach formalism implicitly renormalizes the emitted neutron spectrum. For calculations of neutron evaporation, the denominator is usually dominated by the neutron sum. Changes in the numerator are therefore partially normalized out of the calculation for the sum of the neutron spectrum, even though the sensitivity of the dependence on outgoing energy is maintained.

The Hauser-Feshbach formalism assumes a compound nucleus. A complete theory describing the total reaction cross section should also include direct reaction contributions. For example, there is an indication of a peak in the measured data at about $E_x = 1000$ keV that could not be reproduced by the calculations. This enhancement in the differential cross section exhibits a high degree of angular asymmetry and is likely due to $\ell = 1$ neutrons produced by direct reaction mechanisms. Direct reactions are more likely to produce high-energy neutrons at the low end of the excitation energy spectrum. They are therefore unlikely to account for the discrepancy that is observed at high excitations between the Hauser-Feshbach fit and the measured differential cross section.

V. SUMMARY AND CONCLUSIONS

The first differential cross-section data for the ^{80}Se(γ, n)^{79}Se reaction are reported in this paper. The experiment was carried out at the HIGS, using a linearly polarized γ-ray beam at three incident beam energies: 15.6, 15.8, and 16.0 MeV. The emitted neutrons were detected at reaction angles $(\theta, \phi) = (90°, 180°)$, $(90°, 270°)$, and $(135°, 0°)$. The systematic uncertainty in the differential cross sections reported for each beam energy was about $\pm 10\%$ and was due mostly to the combined effects of the uncertainty in the γ-ray beam flux ($\pm 7\%$), the efficiency of the neutron detectors ($\pm 4\%$), and the correction for the effective neutron transmission from the target to the detector ($\pm 5\%$).

For each γ-ray beam energy, the angle-correlated differential cross-section data were simultaneously fit using the formalism of Weller *et al.* [12,13] to determine the reaction reduced matrix elements as a function of the excitation energy in ^{79}Se. Good fits to the excitation data were obtained with the assumption of a pure $E1$ electric dipole γ-ray excitation in ^{80}Se and with the neutron orbital angular momentum limited to $\ell = 0$ or 1. These results suggest that this reaction is most sensitive to the level densities of the $J = 1/2^-$, $3/2^-$, and $1/2^+$ states in ^{79}Se at the excitation energies accessible with the beam energies of these measurements. The reduced matrix elements extracted at each beam energy were used to calculate the (γ, n) excitation energy spectra.

Empirical fits to the excitation spectra were integrated over energy to estimate the total (γ, n) reaction cross sections. The behavior of the cross section at excitation energies beyond the detector threshold was extrapolated to perform the integration over the entirety of allowed energies. The average uncertainty of the reported total (γ, n) cross sections is $\pm 14\%$. Our total (γ, n) cross sections are 0.8–1.3 standard deviations lower than previously published data [14,15].

The excitation spectra were fit with differential cross sections calculated using a Hauser-Feshbach statistical model. The shape of the data can be described at low excitation energies using level densities in ^{79}Se calculated with a constant-temperature formula and nuclear temperature of 0.7 MeV.

TABLE IV. This table lists the level densities for ^{79}Se as a function of excitation energy (E_x) for the Hauser-Feshbach fits to our angle-integrated (γ, n) cross-section data. The constant-temperature densities (ρ_{bf}) are computed with the parameters that produced the best fit to the data. These level densities are for the aggregate of the J^π states reached by $\ell \leqslant 5$ neutron emission. The level densities computed using Fermi-gas models are normalized to the best fit and listed as $\rho(E_x)/\rho_{bf}(E_x)$. The χ^2 per datum (χ^2/N) for the Hauser-Feshbach fit of the cross-section data using each level-density model is given at the bottom of the column. The references for the Fermi-gas level density models are given in the table header.

E_x (MeV)	Best Fit (ρ_{bf}) (1/MeV)	Rohr [34] ($\times$Best Fit)	Al-Quarishi [35] ($\times$Best Fit)	Iljinov [36] ($\times$Best Fit)	von Egidy [19] ($\times$Best Fit)	Goriely [37] ($\times$Best Fit)
1	4.2					
2	17.4	.15	.14	.34	4.19	1.11
3	72.7	.135	.135	.49	2.80	.92
4	303	.13	.13	.54	1.87	.62
5	1265	.11	.12	.71	1.25	.44
6	5280	.13	.10	.8	.84	.20
χ^2/N	2.09	7.11	7.25	12.6	33.7	38.7

The parameters of the constant-temperature model are consistent with those found by von Egidy and Bucurescu [19] for medium mass nuclei. However, the Hauser-Feshbach fit diverged from the measured data at excitation energies above 5000 keV. Hauser-Feshbach calculations with a Fermi-gas model for the nuclear level density did not describe the data as well as the calculations with a constant-temperature level density. This result is consistent with previous studies of nuclei in this mass region [19].

Measurements of the ^{80}Se(γ, n)^{79}Se reaction at γ-ray beam energies near the reaction threshold are important for understanding stellar synthesis of heavy nuclei and for applications in nuclear waste transmutation. Our method for measuring the (γ, n) reaction cross section provides the first sensitivity to neutron angle correlation and energy dependence.

[1] E. M. Burbidge, G. R. Berbidge, W. A. Fowler, and F. Hoyle, Rev. Mod. Phys. **29**, 547 (1957).

[2] G. Walter, H. Beer, F. Käppeler, and R.-D. Penzhorn, Astron. Astrophys. **155**, 247 (1986).

[3] G. Walter, H. Beer, F. Käppeler, G. Reffo, and F. Fabbri, Astron. Astrophys. **167**, 186 (1986).

[4] F. Käppeler, H. Beer, and K. Wisshak, Rep. Prog. Phys. **52**, 945 (1989).

[5] A. Makinaga, H. Utsunomiya, S. Goriely, T. Kaihori, S. Goko, H. Akimune, T. Yamagata, H. Toyokawa, T. Matsumoto, H. Harano, H. Harada, F. Kitatani, Y. K. Hara, S. Hohara, and Y.-W. Lui, Phys. Rev. C **79**, 025801 (2009).

[6] G. A. Bartholomew, E. D. Earle, A. J. Ferguson, J. W. Knowles, and M. A. Lone, *Advances in Nuclear Physics* edited by M. Baranger and E. Vogt (Plenum Press, New York, 1973), Vol. 7, p. 229.

[7] C. Djalai, N. Marty, M. Morlet, A. Willis, J. C. Jourdain, N. Anantaraman, G. M. Crawley, A. Galonsky, and P. Kitching, Nucl. Phys. A **388**, 1 (1982).

[8] R. Capote, M. Herman, P. Obložinský, P. G. Young, S. Goriely, T. Belgya, A. V. Ignatyuk, A. J. Koning, S. Hilaire, V. A. Plujko, M. Avrigeanu, O. Bersillon, M. B. Chadwick, T. Fukahori, Zhigang Ge, Yinlu Han, S. Kailas, J. Kopecky, V. M. Maslov, G. Reffo, M. Sin, E. Sh. Soukhovitskii, and P. Talou, Nucl. Data Sheets **110**, 3107 (2009); available online at http://www-nds.iaea.org/RIPL-3/

[9] A. Bohr and B. Mottelson, *Nuclear Structure* (Benjamin, New York, 1969), Vol. I, p. 169.

[10] H. Utsunomiya, K. Y. Hara, S. Goko, H. Akimune, T. Yamagata, M. Ohta, H. Ohgaki, H. Toyokawa, T. Hayakawa, T. Shizuma, P. Mohr, Y.-W. Lui, H. Ohkuma, H. Yonehara, K. Soutome, and M. Arnould, Nucl. Phys. A **738**, 136 (2004).

[11] B. Singh, Nucl. Data Sheets **135**, 193 (2016).

[12] H. R. Weller, J. Langenbrunner, R. M. Chasteler, E. L. Tomusiak, J. Asai, R. G. Seyler, and D. R. Lehman, At. Data Nucl. Data Tables **50**, 29 (1992).

[13] H. R. Weller, R. M. Chasteler, B. S. Marks, R. G. Seyler, and D. R. Lehman, At. Data Nucl. Data Tables **58**, 219 (1994).

[14] P. Carlos, H. Beil, R. Bergère, A. Fagot, A. Leprêtre, A. Veyssière, and G. V. Solodukhov, Nucl. Phys. A **258**, 365 (1976).

[15] A. M. Goryachev and G. N. Zalesny, *Voprosy Teoreticheskoy i Yadernoy Fiziki* [Questions in Theoretical and Nuclear Physics] **8**, 121 (1982).

[16] A. J. Koning, S. Hilaire, and M. C. Duijvestijn, "TALYS-1.0", in Proceeding of the International Conference on Nuclear Data for Science and Technology 2007 (EDP Sciences Nice, 2008), p. 211, also see http://www.taly.eu

[17] M. Guttormsen, M. Aiche, F. L. Bello Garrote, L. A. Bernstein, D. L. Bleuel, Y. Byun, Q. Ducasse, T. K. Eriksen, F. Giacoppo, A. Görgen, F. Gunsing, T. W. Hagen, B. Jurado, M. Klintefjord,

A. C. Larsen, L. Lebois, B. Leniau, H. T. Nyhus, T. Renstrøm, S. J. Rose, E. Sahin, S. Siem, T. G. Tornyi, G. M. Tveten, A. Voinov, M. Wiedeking, and J. Wilson, Eur. Phys. J. A **51**, 170 (2015).

[18] A. Gilbert and A. G. W. Cameron, Can. J. Phys. **43**, 1446 (1965).

[19] T. von Egidy and D. Bucurescu, Phys. Rev. C **80**, 054310 (2009).

[20] H. R. Weller, M. Ahmed, H. Gao, W. Tornow, Y. K. Wu, M. Gai, and R. Miskimen, Prog. Part. Nucl. Phys. **62**, 257 (2009).

[21] C. Sun and Y. K. Wu, Phys. Rev. ST Accel. Beams **14**, 044701 (2011).

[22] T. Goorley, M. James, T. Booth, F. Brown, J. Bull, L. J. Cox, J. Durkee, J. Elson, M. Fensin, R. A. Forster, J. Hendricks, H. G. Hughes, R. Johns, B. Kiedrowski, R. Martz, S. Mashnik, G. McKinney, D. Pelowitz, R. Prael, J. Sweezy, L. Waters, T. Wilcox, and T. Zukaitis, Nucl. Technol. **180**, 298 (2012).

[23] J. H. Hubbell and S. M. Seltzer, *Tables of X-Ray Mass Attenuation Coefficients and Mass Energy-Absorption Coefficients* (National Institute of Standards and Technology, Gaithersburg, 2004), Version 1.4. Available online at: http://physics.nist.gov/xaamdi

[24] G. Dietze and H. Klein, *NRESP4 and NEFF 4 Monte Carlo Codes for the Calculation of Neutron Response Functions and Detection Efficiencies for NE 213 Scintillation Detectors* (Physikalisch-Technische Bundesanstalt, Braunschweig, 1982).

[25] M. Chadwick, M. Herman, and P. Obložinský *et al.*, Nucl. Data Sheets **112**, 2887 (2011), special issue on ENDF/B-VII.1 Library.

[26] P. E. Hodgson, *Nuclear Reactions and Nuclear Structure* (Oxford University Press, London, 1971).

[27] A. M. Goryachev, G. N. Zalesny, S. F. Semenko, and B. A. Tulupov, Yadernaya Fizika [Nuclear Physics] **17**, 463 (1973).

[28] A. M. Goryachev, G. N. Zalesny, B. A. Tulupov, Izvestiya Akademii Nauk SSSR, Seriya Fizicheskaya [Proceedings of the Academy of Science of the Soviet Union, Physical Series] **39**, 134 (1975).

[29] F. Kitatani, H. Hrada, S. Goko, H. Utsunomiya, H. Akimune, T. Kaihori, H. Toyokawa, and K. Yamada, Nucl. Sci. Tech. **47**, 367 (2010).

[30] W. Hauser and H. Feshbach, Phys. Rev. **87**, 366 (1952).

[31] S. M. Grimes, Ohio University Internal Report, INPP 04-03, 2004.

[32] A. J. Koning and J. P. Delaroche, Nucl. Phys. A **713**, 231 (2003).

[33] L. McFadden and G. R. Satchler, Nucl. Phys. **84**, 177 (1966).

[34] G. Rohr, Zeit. fur Physik A **318**, 299 (1984).

[35] S. I. Al-Quraishi, S. M. Grimes, T. N. Massey, and D. A. Resler, Phys. Rev. C **67**, 015803 (2003).

[36] A. S. Iljinov, M. V. Mebel, N. Bianchi, E. De Sanctis, C. Guaraldo, V. Lucherini, V. Muccifora, E. Polli, A. R. Reolon, and P. Rossi, Nucl. Phys. A **543**, 517 (1992).

[37] S. Goriely, S. Hilaire, and A. J. Koning, Phys. Rev. C **78**, 064307 (2008).